Charge-density oscillations on Be($10\bar{1}0$): Screening in a non-free two-dimensional electron gas

B. G. Briner
Fritz-Haber-Institut der Max-Planck-Gesellschaft, Faradayweg 4-6, D-14195 Berlin

Ph. Hofmann*
Fritz-Haber-Institut der Max-Planck-Gesellschaft, Faradayweg 4-6, D-14195 Berlin;
Department of Physics and Astronomy, University of Tennessee, Knoxville, Tennessee 37888;
and Oak Ridge National Laboratories, Oak Ridge, Tennessee 37800-1501

M. Doering and H.-P. Rust
Fritz-Haber-Institut der Max-Planck-Gesellschaft, Faradayweg 4-6, D-14195 Berlin

E. W. Plummer
Department of Physics and Astronomy, University of Tennessee, Knoxville, Tennessee 37888
and Oak Ridge National Laboratories, Oak Ridge, Tennessee 37800-1501

A. M. Bradshaw
Fritz-Haber-Institut der Max-Planck-Gesellschaft, Faradayweg 4-6, D-14195 Berlin
(Received 30 April 1998)

The surface state on Be($10\bar{1}0$) has been investigated using a low-temperature scanning tunneling microscope (STM). The Fermi contour of this surface state is located at one boundary of the surface Brillouin zone, and surface-state electrons provide the main part of the charge density near the Fermi energy. Be($10\bar{1}0$), therefore, corresponds closely to a non-free two-dimensional electron gas. We have observed standing waves of the surface charge density on Be($10\bar{1}0$) near step edges and point defects. Such wave patterns derive from the interference of incoming and scattered electrons; they demonstrate the screening characteristics of the surface state. On Be($10\bar{1}0$) these waves were found to be highly anisotropic. It is shown that calculating the Fourier transforms of topographic STM images is a powerful method for determining the Fermi contour of the surface state. This method could even be applied to images that display a complex wave pattern arising from a random distribution of point scatterers. Fourier analysis also revealed that the charge density oscillations on Be($10\bar{1}0$) contain multiple periods that differ by reciprocal lattice vectors. These multiperiodic oscillations relate to the non-free character of the surface-state electrons and constitute an interference pattern of Bloch states. Fourier filtering was used to separate the charge-density oscillations from the topographic corrugation and to visualize their shape and spatial range. The experimental data are qualitatively discussed using a model calculation based on the scattering of Bloch electrons from planar obstacles in a two-dimensional conductor. Experimental results and model calculations highlight how the screening characteristics on Be($10\bar{1}0$) significantly deviate from the behavior expected for a free two-dimensional electron gas. [S0163-1829(98)08143-0]

I. INTRODUCTION

When an impurity is introduced into a metal the conduction electrons try to screen this localized excess charge. Screening leads to a perturbation of the conduction electron density in the vicinity of the impurity, the shape of which depends critically on the metallic band structure. It was first shown by Friedel[1] that a point scatterer embedded in a free-electron gas induces a long-range *oscillatory* perturbation of the total charge density. This so-called Friedel oscillation extends rather far out from the impurity site; for a three-dimensional electron gas the excess charge $\delta\rho$ decays according to $\delta\rho \propto (k_F/r^3)\cos 2k_F r$ (k_F is the Fermi wave vector). Due to reduced dimensionality, the range of the Friedel oscillations becomes even more extended on surfaces and in thin films.[2,3] Friedel oscillations also mediate an indirect interaction between two adjacent scatterers (e.g., between adsorbed particles) which exhibits the same oscillatory behavior and extended range.[4] Such indirect interactions can have important implications for adsorption-related phenomena such as the formation of ordered superstructures. The oscillatory character of $\delta\rho$ derives from the wave-vector dependence of the dielectric susceptibility $\epsilon(q)$. For a free-electron metal $\epsilon(q)$ strongly decreases for $q > 2k_F$, i.e., a free-electron metal is not able to effectively screen a perturbation potential with Fourier components q larger than the diameter of the Fermi sphere. In addition to being responsible for the Friedel oscillations, the susceptibility cutoff at $2k_F$ also gives rise to a discontinuity in the phonon spectrum.[5]

The experimental imaging of Friedel oscillations has only recently become possible. In 1993, two research groups reported the observation of charge-density oscillations of the Shockley-type surface state on Cu(111) and Au(111).[6,7] Both

groups used a scanning tunneling microscope (STM) to probe the local-surface charge density near the Fermi level with high-lateral resolution. Crommie *et al.* also managed to build beautiful nanostructures, which act as resonators for the surface-state electrons and allow the resonant modes to be resolved in real space.[8] After these pioneering studies, similar oscillations were observed on Be(0001),[9] Ag(111),[10] in argon bubbles,[11] and near dopants on GaAs(110).[12] All these data share in common that the investigated surface states exhibit the characteristics of free electrons, i.e., their Fermi contour corresponds to a circle centered at the $\bar{\Gamma}$ point of the surface Brillouin zone. For this reason the observed wave patterns have been isotropic and contain only one period.

While experimental data on charge-density oscillations are still sparse, a large number of studies have been performed on a closely related topic, the indirect magnetic-exchange coupling. The same screening process that is responsible for the Friedel oscillations also leads to an oscillatory perturbation of the spin density in the vicinity of a magnetic impurity. This perturbation mediates a spin-dependent interaction between two impurities, which is usually termed the Ruderman-Kittel-Kasuya-Yosida (RKKY) interaction.[13] Spin density oscillations could not yet be imaged because of the lack of a suitable spin-resolved microscopy, but the RKKY interaction is observable. It leads to either parallel or antiparallel alignment of the magnetization in ferromagnetic films, which are separated by a nonmagnetic layer.[14,15] The oscillatory character of this interaction is most directly revealed in experiments with wedge-shaped spacer layers.[16,17] For several spacer materials it was found that the coupling exhibits multiple oscillation periods. Theoretical investigations have indicated that such multiperiodic oscillations derive from the non-free character of the conduction electrons; they reflect the band structure of the spacer material.[18–20]

Although the links between multiperiodicity and band structure have already been established for the case of magnetic coupling, it is still desirable to search for similar effects in the STM-based experiments on charge-density oscillations. Such STM experiments are much less restrictive than the observation of magnetic coupling in heterostructures. While at present the RKKY interaction can be probed only along the growth direction of the heterostructure and for distances r corresponding to multiples of the lattice period, the STM captures all possible wave vectors of the surface state in just one image. Here we confirm that it is possible to image charge-density oscillations of a *non-free* electron gas with a low-temperature STM. It is shown how the shape of the observed wave patterns reflects the band structure of the surface state under investigation. This paper complements and extends two shorter reports that have focused on the anisotropy[21] and multiperiodicity[22] of the charge-density oscillations on Be$(10\bar{1}0)$. The remainder of the paper is organized as follows. In Sec. II it is explained why we have chosen Be$(10\bar{1}0)$ for these experiments, and, in addition, some technical details about our experimental setup are provided. Section III presents topographic STM images and Fourier spectra of charge-density oscillations. In a second part of this section we show how Fourier filtering can be used to analyze the charge-density oscillations in more detail. The discussion in Sec. IV is devoted to a simplified theoretical model that qualitatively reproduces the observed wave patterns at step edges, kinks, and point defects.

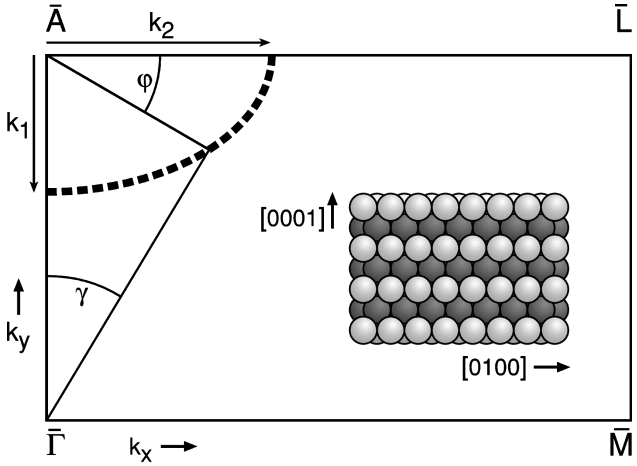

FIG. 1. Irreducible part of the surface Brillouin zone of Be$(10\bar{1}0)$ together with the surface Fermi contour (dashed line); a real-space view of Be$(10\bar{1}0)$ is shown in the inset. This sketch defines coordinate axes and several additional variables that are used in Sec. IV.

II. EXPERIMENT

A. Be$(10\bar{1}0)$ surface

The beryllium atom has a simple electronic structure $(1s^2 2s^2 2p^0)$, but the physical properties of solid beryllium differ in many respects from those of other simple metals. Electronic structure calculations for bulk Be (Ref. 23) have shown that the $2s$ valence electrons are, to a large degree, promoted into $2p$ states. The bulk density of states (DOS) displays a pronounced dip at the Fermi energy ϵ_F, which makes electron dynamics near ϵ_F differ significantly from the free-electron model. Both experimental and theoretical studies have indicated that the properties of the (0001) and $(10\bar{1}0)$ Be surfaces are largely influenced by the presence of surface states. These states lie in wide band gaps and exhibit a high degree of localization in the surface atomic layer. They contribute the main part of the surface charge density because of the low density of the projected bulk states. Be(0001) and Be$(10\bar{1}0)$, therefore, correspond closely to the model system of a two-dimensional electron gas. On both surfaces it has been observed that core-level shifts contain contributions from the first three surface layers,[24] while in other metals such shifts are usually confined to the topmost atomic layer. The surface state on Be(0001) was investigated by means of angle-resolved photoemission[25] and STM.[9] In accordance with self-consistent pseudopotential calculations[26] it was found that the surface state on Be(0001) is centered at the $\bar{\Gamma}$ point of the surface Brillouin zone (SBZ) and exhibits free-electron-like parabolic dispersion.

For Be$(10\bar{1}0)$, model calculations have indicated the existence of a surface state at the edge of the SBZ (see Fig. 1).[27] It was predicted that the Fermi contour of this state consists of two semielliptic segments centered at $\bar{A}$. Subse-

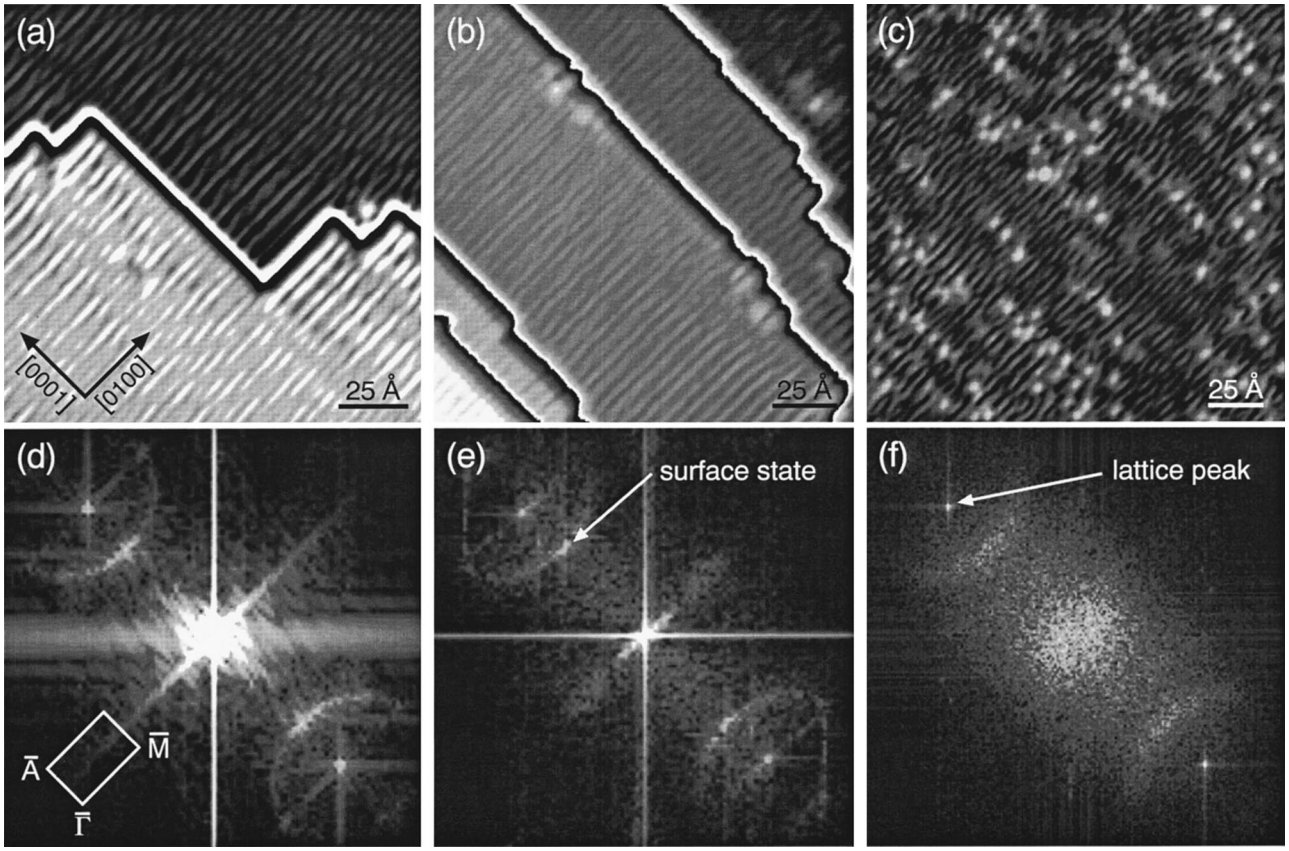

FIG. 2. (a)–(c) Topographic STM images of the Be(10$\bar{1}$0) surface. All images were recorded with a tunnel current of 100 pA. The sample bias-voltage V_b was -10 mV for (a), -25 mV for (b), and $+20$ mV for (c), respectively. (d)–(f) Power spectra (logarithmic scale) of the STM topographs shown above. All three spectra display the Fermi contour of the surface state (semielliptic line) and a peak at $\bar{A}$ that derives from the lattice. The inset in (d) shows the irreducible part of the surface Brillouin zone on Be(10$\bar{1}$0).

quently, the surface state on Be(10$\bar{1}$0) was investigated at room temperature by means of angle-resolved ultraviolet photoemission spectroscopy (ARUPS).[28] A comparison of ARUPS results and first-principles calculations indicated that the Be(10$\bar{1}$0) surface terminates in the configuration with a short spacing between the first two atomic layers. This finding is in agreement with a low-energy electron diffraction (LEED) study on the same surface.[29] At room temperature, the bottom of the surface-state band was found to lie 320 meV below E_F, and the radii of the Fermi contour were determined to be 0.22 Å^{-1} in the $\bar{\Gamma}$-$\bar{A}$ direction and 0.31 Å^{-1} in the $\bar{A}$-$\bar{M}$ direction[28] The surface state on Be(10$\bar{1}$0) does *not* correspond to the free-electron model, because its band bottom is offset from the center of the SBZ, and because the wave vector k decreases with increasing energy. This deviation from free-electron dynamics, together with the dominance of surface-state electrons in the charge density near ϵ_F, make Be(10$\bar{1}$0) an attractive model surface for studying the correlation between electronic structure and screening characteristics in real space.

B. Technical details

All experimental results of this study have been obtained using a low-temperature ultrahigh-vacuum STM that was built after a design of Weiss and Eigler.[30] The instrument contains a mechanical-approach mechanism[31] and can be operated at variable temperatures down to 3 K. To obtain the lowest possible noise level and to keep the sample surface clean for extended measuring periods we have recorded all STM data at $T \approx 5$ K. A commercially available PtIr tip was used in these experiments. The tip was prepared *in situ* either by applying voltage pulses of up to 10 V or by gently indenting the tip into the sample surface. As a consequence, the chemical identity of the last atom at the tip apex is unknown. All images were recorded in the constant-current mode with a tunneling current of 100 pA. In order to obtain at the same time a high-lateral resolution and a satisfactory k-space resolution we have acquired rather large (1000 $\times$1000 pixel) images with a pixel raster of typically 0.3–0.5 Å. Prior to the experiments, the Be(10$\bar{1}$0) crystal was cleaned by repeated cycles of argon-ion sputtering and subsequent flash annealing to 900 K until no oxygen could be detected in the Auger electron spectrum (AES). Although annealing at higher temperatures and for a prolonged time resulted in an improved LEED pattern, we preferred to keep annealing times short in order to avoid surface segregation of bulk contaminants (mainly Si according to AES). A further experimental problem was the substantial roughness of our Be(10$\bar{1}$0) crystal. Upon annealing the surface formed ex-

tended pyramidal structures. Therefore, it was difficult to find large atomically flat terraces, which are needed to study the decay of charge-density oscillations near step edges.

III. RESULTS

Charge-density oscillations on Be$(10\bar{1}0)$ were always found to be remarkably anisotropic. This is illustrated in Figs. 2(a)–2(c) for three different scattering geometries. All three images show essentially raw topographic data. The only processing that has been performed on Fig. 2(a) and 2(b) is a partial subtraction of the step height. This processing leaves the waves undistorted, but it transforms the step edges to pairs of parallel black and white lines. Step subtraction has been performed to reduce the gray scale range in the printed images. The same processing has been used throughout this paper wherever it was necessary to reduce the z range of an image. Figure 2(a) displays two terraces separated by a zigzag-shaped step edge. The wave fronts that appear on both terraces of Fig. 2(a) are almost exclusively oriented parallel to the [0100] direction. The segments of the step edge that run parallel to [0001] seem to be very inefficient scatterers because almost no waves originate at these steps. This can be seen more clearly on the surface segment shown in Fig. 2(b). Although this image contains several long [0001] steps, the wave fronts on Fig. 2(b) all run parallel to [0100]. Figure 2(c) illustrates the shape of the charge-density oscillations on a surface with a random distribution of point scatterers. This image has been recorded after prolonged annealing of the Be$(10\bar{1}0)$ crystal. The bright spots are bulk impurities that have segregated to the surface as a result of the annealing process. The wave pattern in Fig. 2(c) is quite complex, but one can still recognize the preferential orientation of the wave fronts parallel to the [0100] direction.

Fourier transforming of the topographic data proved to be very useful for analyzing the shape of the charge-density oscillations. This technique was first used for extracting the periodicity of incommensurate charge-density waves from the STM images of TaS_2.[32] Sprunger *et al.* have shown that the application of Fourier transform analysis to the STM images (FTSTM) is also a powerful tool for investigating surface states.[9,33] Figures 2(d) and 2(f) demonstrate that the Fermi contour of Be$(10\bar{1}0)$ can be visualized using FT-STM. These three images display the power spectra (logarithmic scale) of the topographic data shown in the top row of Fig. 2. Two peaks and two semielliptic lines are discernible in all power spectra. The peaks indicate that the lattice corrugation in the [0001] direction is resolved in the STM. On one hand, these lattice peaks are convenient because they facilitate the lateral calibration of the STM images. On the other hand, the lattice peaks complicate the interpretation of the wave patterns, because they indicate that the charge-density oscillations are superimposed onto a topographic background. We denote the corrugation with lattice periodicity as ''topographic'' to distinguish it from the components of the charge-density oscillations that are incommensurate with the lattice. It should, however, be emphasized that on Be$(10\bar{1}0)$ the topographic corrugation derives not only from projected bulk states but also from the lattice periodic terms

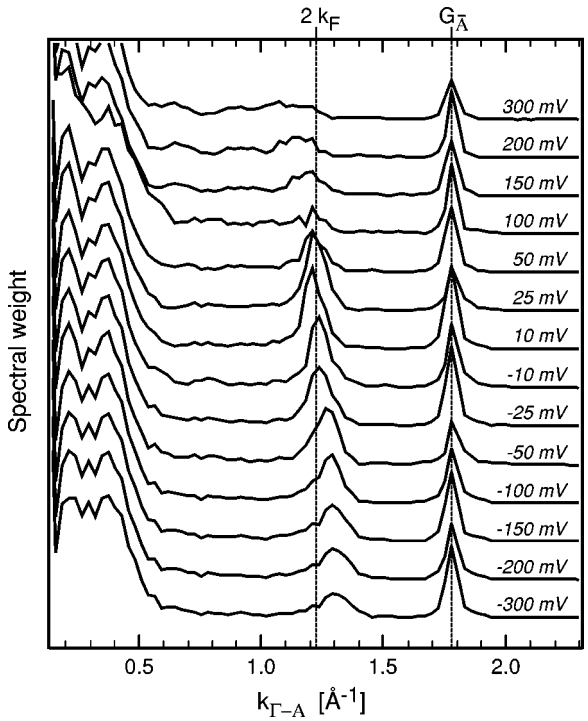

FIG. 3. Cross sections in the $\bar{\Gamma}$-$\bar{A}$ direction extracted from spectral images that were recorded with different bias voltages. All power spectra represent the wave pattern of the same 163 Å $\times$ 163 Å sample area. The lattice peak at $G_{\bar{A}}$ and the position of the surface-state peak at ϵ_F are marked. Curves are labeled by the sample bias voltage.

of the charge-density oscillations (cf. Sec. IV and Ref. 21). The semielliptic features in Figs. 2(d) and 2(f) give clear evidence for the presence of charge-density oscillations on Be$(10\bar{1}0)$. Based on the ARUPS data for the surface state on Be$(10\bar{1}0)$,[28] we infer that these semiellipses are a replica of the surface-state Fermi contour. It will be shown in Sec. IV that the power spectrum of the wave pattern in the vicinity of a point scatterer does indeed contain such semielliptic features.

Why do the semiellipses appear in Figs. 2(d) and 2(e) although there are no pointlike impurities on the corresponding topography images? For symmetry reasons, [0100] steps would just emit straight wave fronts that become transformed into a pair of spots on the $\bar{\Gamma}$-$\bar{A}$ axis in the power spectrum. We postulate that the semiellipses are fully visible because the kinks of the step edge act as pointlike scatterers. By distorting the straight wave fronts that emanate from adjacent step edges the kinks contribute to the spectral weight in the tails of the semiellipses. The power of the FTSTM becomes particularly evident from Figs. 2(c) and 2(f). Although in this example the topographic image displays a complex superposition of wave trains originating from multiple impurities, it is still possible to recognize the semielliptic Fermi contour in the power spectrum.

In Fig. 3 it is shown how the power spectrum of the charge-density oscillations on Be$(10\bar{1}0)$ depends on the bias voltage. This graph contains a series of line cuts across Fourier images. All cuts display the spectral weight in the $\bar{\Gamma}$-$\bar{A}$ direction. The lattice peak at $G_{\bar{A}}=2k_{\bar{A}}$ and the surface-state

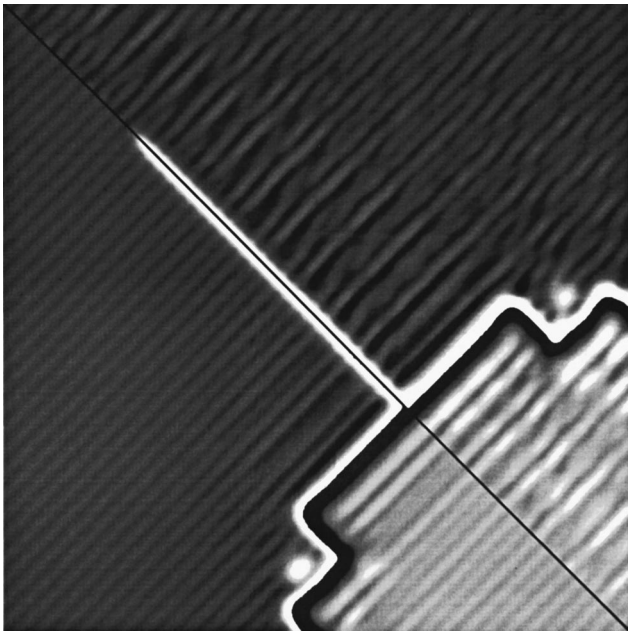

FIG. 4. Comparison of the wave patterns in STM topographs with different bias voltages. This composite image (145 Å $\times$145 Å) has been assembled from two data sets of the same surface area. The segment shown in the upper-right triangle was recorded with $V_b=-10$ mV, i.e., it represents the energy-resolved charge-density oscillations in the vicinity of the Fermi energy. The lower-left triangle shows the wave pattern (mirror symmetric), which was observed for $V_b=-300$ mV.

peak are both visible. At negative-sample bias (i.e., when the STM probes the occupied states on the sample) the surface-state peak is offset towards the lattice peak compared to its position at the Fermi level. With increasing sample bias the surface-state shifts towards the center of the Brillouin zone. Figure 3 obviously shows that the wave vector k of the surface state decreases with increasing energy, i.e., it *qualitatively* reveals the dispersion characteristics. It is, however, not possible to derive the quantitatively correct dispersion relation from the data shown in Fig. 3. Because the spectra were obtained from topographic images, they represent a weighted integral of the density of states from the Fermi energy ϵ_F to the bias level.[34,35] In principle, the differential conductivity dI_T/dV_b would provide a good approximation to the local density of states at the bias level, but to record large dI_T/dV_b images is very time consuming. Several researchers have relied on conductivity data to investigate in detail the dispersion of free-electron-like surface states.[6,7,10] These experiments could benefit from the isotropic shape of the free-electron charge-density oscillations (when the waves look the same for all propagation directions it is sufficient to record dI_T/dV_b on a line starting at a step edge). Such a shortcut is not possible on Be(10$\bar{1}$0) because of the pronounced anisotropy of the charge-density oscillations. It should be mentioned that even using conductivity data it is rather delicate to derive correctly the shape of the density of states.[35,36] For Ag(111) it has been shown that the density of states can be extracted from an analysis of simultaneously recorded topography and conductivity data.[10] In this study it was also substantiated that for low-bias voltages, current (or topography) images provide a better approximation to the true density of states than conductivity images. Comparing the FTSTM with ARUPS we find that these two methods for investigating surface states exhibit complementary strengths. Distinct advantages of the FTSTM are the ability to quickly image the Fermi surface and to probe unoccupied states above ϵ_F. We do, however, consider ARUPS as the method of choice for measuring the dispersion of occupied bands that extend more than a few 100 meV below ϵ_F. In this energy range the large photoelectron yield makes it relatively straightforward to perform an ARUPS experiment whereas the FTSTM data become increasingly difficult to interpret because of the unknown electronic structure of the probe tip.

The wave patterns that are observed in topographic STM images are often described as ''Friedel oscillations,'' although this is not entirely correct. The true Friedel oscillation is a perturbation of the *total* charge density, whereas STM images at low-bias voltage display oscillations of the *energy-resolved* charge density near ϵ_F. The physics behind both oscillatory perturbations is, however, identical. We therefore consider it justified to use the term Friedel oscillation in a somewhat generalized sense. The major difference between energy-resolved and ''true'' Friedel oscillations is their spatial range. This is illustrated in Fig. 4, a composite image that has been assembled from two data sets showing the same surface area. The segment in the upper-right triangle of Fig. 4 was recorded with $V_b=-10$ mV. It displays the energy-resolved charge-density oscillations near ϵ_F. For the data set that is reproduced in the lower-left triangle we have used a sample bias of -400 mV. Apart from a weighting factor due to the variable-tunneling barrier height, this image shows the integrated charge density from the band bottom of the surface state up to ϵ_F,[37] i.e., it approximately displays the true Friedel oscillation. When comparing both data sets we observe that the energy-resolved oscillations extend much farther out from the step edge than the true Friedel oscillations. In the lower-left triangle the Moiré pattern that indicates the superposition of lattice contrast and charge-density oscillations appears only in the immediate vicinity of the step edge. In contrast, this Moiré pattern is visible on the whole area of the image in the upper-right triangle. The longer range of the energy-resolved oscillations relates to the dispersion of the surface state. Because the wavelength of the oscillations varies with energy, destructive interference partially cancels the waves when the energy-resolved charge density is integrated over all occupied states. From the experimental point of view it is advantageous to observe the energy-resolved oscillations rather than the true Friedel oscillations because their extended range creates additional spectral weight in the Fourier image and makes it possible to recognize even weak scatterers. Normally, the wave patterns that appear in the energy-resolved spectra at the Fermi level reflect the nature of the true Friedel oscillations. It must, however, be kept in mind that *any* sharp feature in the band structure creates an oscillatory perturbation of the screening electron density. If such features exist below ϵ_F the Friedel oscillations will contain additional wave vectors. These waves are not associated with the shape of the Fermi contour, and they do not appear in STM images with low bias voltage.

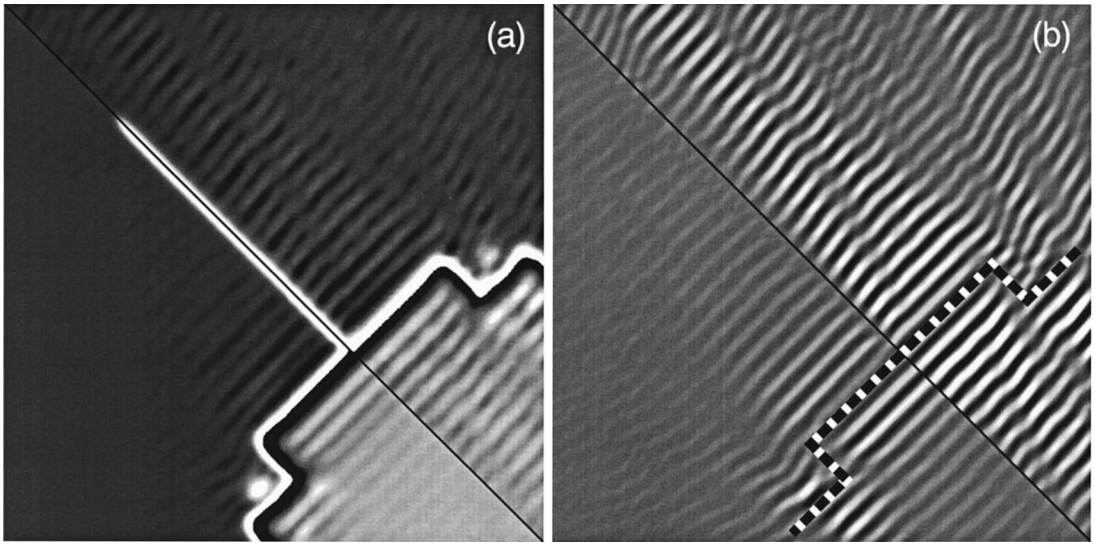

FIG. 5. Same data as shown in Fig. 4 after Fourier filtering. Image (a) has been obtained by suppressing the lattice peaks in the power spectrum. The remaining waves represent exclusively charge-density oscillations of the surface state. For image (b) only a narrow band around the semielliptic features that derive from the surface state has been selected in the power spectrum. Because the step edge is removed by this processing step its position is indicated by a dashed line in (b).

A. Fourier filtering

STM images of Be$(10\bar{1}0)$ always show the Friedel oscillations superimposed on a topographic background. Topographic information and Friedel oscillations both appear as wavelike patterns with ridges running parallel to [0100]. Therefore, it is impossible to determine in detail the shape and spatial range of the Friedel oscillations directly from the raw data. Fortunately, there is a solution to this problem: Fourier filtering. This technique allows individual features of the power spectrum to be selectively enhanced or suppressed. Filtering in the k space is performed by multiplying the complex two-dimensional Fourier transform $\zeta(k_x,k_y)$ of a topographic image $z(x,y)$ with a real filter mask $m(k_x,k_y)$ and subsequently calculating the reverse transform. The filter mask has to be symmetric with respect to $\mathbf{k}=0$. For example, the following mask function is a convenient choice to select a circular region of radius dk centered at $\mathbf{k}_0$ in the power spectrum:

$$m(\mathbf{k})=0.5\left(\frac{1}{1+(|\mathbf{k}-\mathbf{k}_0|/dk)^n}+\frac{1}{1+(|\mathbf{k}+\mathbf{k}_0|/dk)^n}\right). \tag{1}$$

For $\mathbf{k}_0=0$ this function corresponds to an nth order Butterworth lowpass. The inverted mask $\bar{m}(\mathbf{k})=1-m(\mathbf{k})$ can be used in exactly the same way to suppress a circular region around $\mathbf{k}_0$.

One has to be aware of a potential pitfall of Fourier filtering. Steep edges at the cutoff points of the filter mask can introduce oscillatory artifacts in the filtered image. Such artifacts could, in principle, be mistaken for true charge-density oscillations. The mathematics behind filter artifacts and Friedel (or the RKKY) oscillations is formally very similar. This becomes particularly clear from a derivation of the RKKY oscillations via wave-vector dependent screening (the RKKY oscillations appear because of a steep decrease of the wave-vector dependent susceptibility at $2k_F$; see Ref. 38). Although there is no way to ensure that a filtered image is completely free of artifacts, two rules of thumb greatly help to minimize the problem. First, the mask cutoffs should be located in regions of low spectral weight, because the amplitude of the artifacts scales with the spectral density at the location of the filter edges. Second, the edges of the filter mask should be smoothed as much as possible. This confines the remaining artifacts to a narrow range. In practice we find it most convenient to test for artifacts by comparing images that have been processed using different filter masks. Wave patterns that look the same on all images can confidently be assigned to true charge-density oscillations, because the shape of the filter artifacts changes for different mask functions. We note that Fourier filtering of STM images can also be used as a tool for identifying adsorbate sites on metal surfaces by selectively enhancing the lattice corrugation.[39]

In Fig. 5 it is illustrated how the shape of the charge-density oscillations on Be$(10\bar{1}0)$ can be visualized by means of Fourier filtering. Figure 5(a) displays the same data that have been shown in Fig. 4 after suppression of the lattice corrugation. It is now much easier to recognize the long range of the energy-resolved oscillations (upper-right triangle) as compared to the oscillations of the integrated charge density (lower-left triangle). In Fig. 5(b) we have highlighted the contribution of the semielliptic features in the power spectrum. This image was obtained by suppressing all of the power spectrum with the exception of a narrow band around the semiellipses. Figure 5(b) reveals how kinks distort the wave pattern that is promoted at step edges; it can be seen that narrow zones of reduced wave amplitude originate at the kinks. We have postulated that the semielliptic lines in the Fourier images of Figs. 2(d) and 2(e) are fully visible only because of scattering at the kinks. It was, however, almost impossible to verify this statement from the raw-data images. On filtered images like the one shown in Fig. 5(b) it is easy to recognize that kinks ''bend'' the wave fronts emanating from step edges. Such bent wave fronts contribute to the spectral weight that appears in the ''tails'' of the semielliptic Fermi contours.

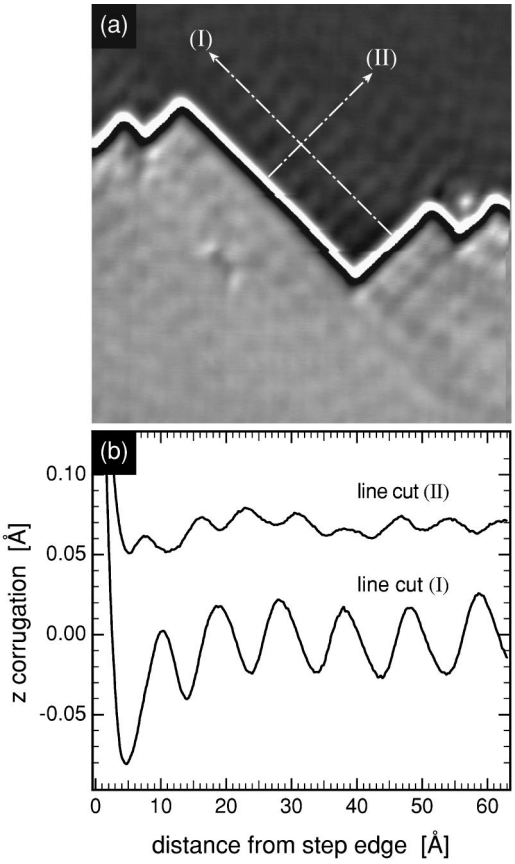

FIG. 6. (a) Fourier-filtered image ($V_b=-10$ mV, 145 Å $\times$145 Å). The lattice peak and the semielliptic feature of the surface state have both been suppressed in the power spectrum. (b) Averaged line cuts across the image shown in (a). The line cuts display charge-density oscillations originating at step edges running parallel to [0100] (i) and [0001] (ii), respectively. The position of the cuts is marked by dashed white lines in (a).

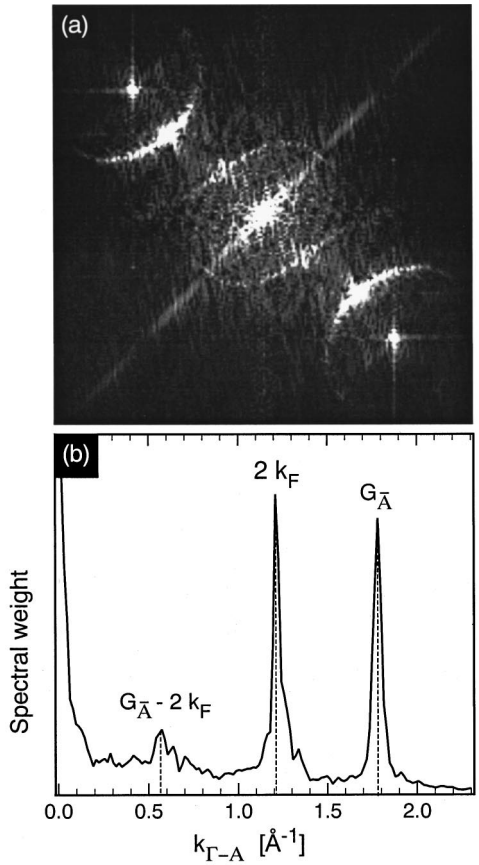

FIG. 7. Multiperiodicity of the charge-density oscillations on Be(10$\bar{1}$0). (a) Power spectrum that was obtained from a 280 Å $\times$280 Å STM topograph ($V_b=-10$ mV, $I_t=100$ pA) after subtracting the step edge. The spectrum displays an additional ellipse in the center that corresponds to the long-period oscillations shown in Fig. 5. The pixel raster in the spectral image is 0.02 Å^{-1}. (b) Line cut in the $\bar{\Gamma}$-$\bar{A}$ direction extracted from the spectrum shown in (a). The additional peak at $G_{\bar{A}}-2k_F$ marks the position of the central ellipse.

A key property of the Friedel oscillations on Be(10$\bar{1}$0) is their multiperiodic shape.[22] By comparing Figs. 5(a) and 5(b) we get a first hint that the waves contain more than just the contribution of the semiellipses around $\bar{A}$. Although the lattice contribution has been removed in both images there remain significant differences between the total wave pattern [Fig. 5(a)] and the part of the waves that derive from the semiellipses [Fig. 5(b)]. To obtain clear evidence that the observed waves contain multiple periods we again resort to Fourier filtering. Figure 6(a) shows the same data that were used for Fig. 4 (upper right) after Fourier filtering with a mask that suppresses both the lattice peaks *and* the semielliptic contours around $\bar{A}$. Judging from the power spectra we would expect that an image that is filtered by this method does not display any waves at all. This is, however, not the case. Figure 6(a) contains waves running in both the [0001] and the [0100] directions. The shape of these waves is further illustrated in Fig. 6(b). This graph displays averaged line cuts that were extracted from Fig. 6(a) along the indicated directions. Line cut I illustrates that the strong waves emanating from [0100] steps contain a long wavelength component in addition to the dominant oscillation at $2k_F$. Line cut II shows that step edges running parallel to [0001] also emit waves, but the amplitude of these oscillations is about a factor of five smaller compared to the waves emanating from [0100] steps.

Why are the additional long period waves not seen in the Fourier images of Fig. 2? These waves are indeed contained in the Fourier spectrum but they are covered up by low-frequency topographic contrast. To visualize the contribution of the additional waves to the power spectrum we have suppressed the topographic contrast by subtracting the step height and blanking out the step edges (see Ref. 22 for details). After processing a topographic image (270 Å $\times$270 Å, $V_b=-10$ mV) with this method we obtain the power spectrum shown in Fig. 7(a). An additional ellipse is clearly present in the center of this image. The new ellipse is shifted by a reciprocal lattice vector with respect to the stronger semielliptic contours around $\bar{A}$. This can be seen more clearly from the line cut across $\bar{\Gamma}$-$\bar{A}$, which is shown in Fig. 7(b). Multiperiodic charge-density oscillations are a fingerprint of the nonfree character of the conduction electrons. The presence of an additional wave period at $G_{\bar{A}}-2k_F$ indicates that the wave functions of the surface-state electrons on Be(10$\bar{1}$0) differ significantly from plane waves, i.e., they

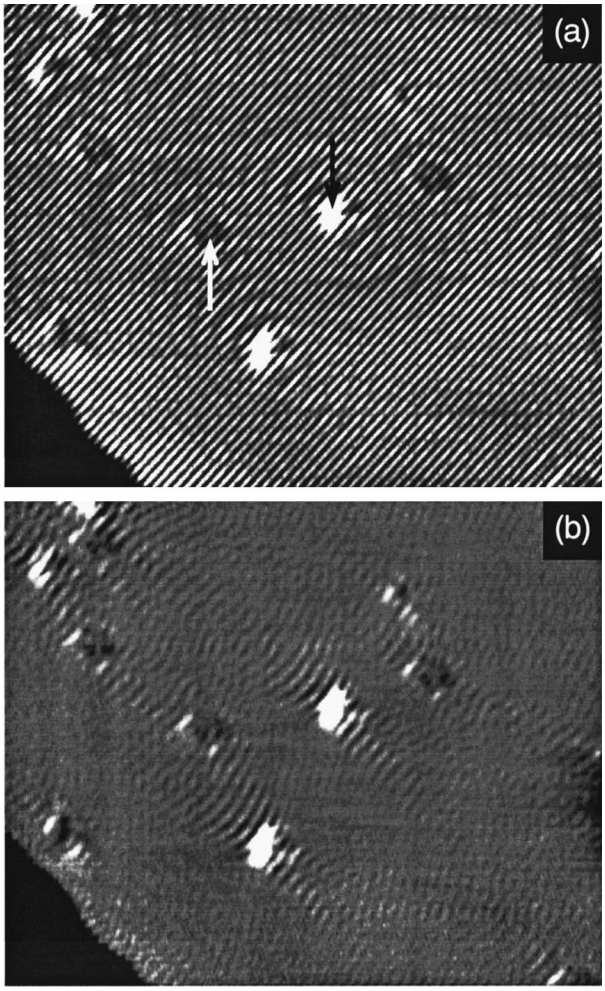

FIG. 8. Charge-density oscillations near pointlike scatterers. (a) Constant current STM image (260Å×210Å, V_b = 40 mV, I_t = 100 pA). The image displays some small clusters (black arrow) and shallow depressions (white arrow). (b) Same data after lattice suppression by means of Fourier filtering. The wave patterns in the vicinity of the surface defects and clusters are visualized. In both images the gray scale spans a z range of ± 0.05Å.

contain higher order Bloch components. From Fig. 7(a) we obtain the following values for the dimensions of the Fermi contour: $k_1 = 0.29 \pm 0.01$ Å^{-1} and $k_2 = 0.39 \pm 0.01$ Å^{-1} (k_1 and k_2 are indicated in Fig. 1). This corresponds to a Fermi wave vector of $k_F = 0.58$ Å^{-1} in the $\bar{\Gamma}$-$\bar{A}$ direction. The dimensions of the Fermi contour are in good agreement with first principles calculations, but they are significantly larger than the results that were obtained by means of ARUPS.[29] Figure 6 has been calibrated using the theoretically derived value of $G_{\bar{A}} = 1.78$ Å^{-1}. If the experimental room-temperature result[40] for $G_{\bar{A}}$ was used instead, all wave vectors would have to be scaled down by a factor of 0.98. The peak representing the centered elliptical contour in Fig. 7(b) is located at 0.57 Å^{-1}, in accordance with the expectation that it should appear at $k = G_{\bar{A}} - 2k_F$.

B. Point defect

So far we have concentrated on the shape of Friedel oscillations near step edges. The reader might, however, argue that a point impurity and not a step is the simplest possible scatterer. The reason for focusing mainly on step edges is purely technical. It proved to be difficult to prepare a Be$(10\bar{1}0)$ surface with a low density of point scatterers. Our setup did not allow for metal evaporation,[6,8] and the adsorption of small molecules (O_2, CO) from the gas phase failed due to a very low sticking coefficient on Be$(10\bar{1}0)$. Finally, we had to resort to surface segregation of bulk impurities. A main disadvantage of this method is the difficulty to control the impurity concentration via annealing time and temperature. A typical result that was obtained using the segregation method is shown in Fig. 8. The topographic image in Fig. 8(a) displays some adsorbed particles or clusters (black arrow). In addition, several impurities appear as shallow depressions (white arrow). We speculatively assign these features to subsurface impurities. Although the gray scale of Fig. 8(a) is limited to a narrow z range, it is almost impossible to recognize charge-density oscillations near the impurities; the contrast is dominated by the lattice contribution. Here, Fourier filtering proves indispensable to extract the shape of the Friedel oscillations. Figure 8(b) shows the same image after suppression of the lattice peak. We recognize wave fronts emanating from all impurities. The waves are again very anisotropic, in accordance with what has been found for the step edges. Perhaps the most striking property of the waves is their negative curvature. As the wave fronts bend away from the scatterer, they look like replicas of the semielliptic Fermi contour. This result contrasts with the shape of the Friedel oscillations in free-electron-like systems where a point defect gives rise to circular wavelets. Figure 8(b) illustrates that even scattering from a point defect that may seem simple for free electrons can become rather intricate for non-free-electron systems. Finally, we note that Fig. 8(b) also displays weak charge-density oscillations emanating from the [0001] step in the lower-left corner. This result confirms our finding that the [0001] steps scatter only very inefficiently.

IV. DISCUSSION

The aim of this section is to demonstrate that the main features of the observed charge-density oscillations (anisotropy, multiperiodicity) derive directly from the non-free electron character of the surface state. The wave function of a surface-state electron can be written as[34]

$$\psi_{\mathbf{k}}(\mathbf{r}_{||},z) = \sum_{\mathbf{G}} a_G \exp\{-[\kappa^2 + (\mathbf{k}_{||}+\mathbf{G})^2]^{1/2} z\} \times \exp[i(\mathbf{k}_{||}+\mathbf{G})\cdot\mathbf{r}_{||}]. \quad (2)$$

Here, $\kappa = \hbar^{-1}\sqrt{2m(\phi + \epsilon_F - \epsilon)}$ is the decay length into the vacuum, ϕ denotes the work function, ϵ_F the Fermi energy, and ϵ the electron energy with respect to the band bottom of the surface state. $\mathbf{k}_{||}$ is the parallel wave vector and $\mathbf{G}$ an arbitrary reciprocal lattice vector. The surface is located at $\mathbf{r}_{||} = (x,y,0)$, and the STM samples the surface state at a distance of $z \approx 5$ Å above the surface.

Below we use the simplest possible description of scattering at step edges, total reflection by a hard wall. In this approximation the reflected wave function ψ_{out} is obtained by inverting the incoming wave ψ_{in} [e.g., for a step edge at $y = 0$ we get $\psi_{out}(x,y) = -\psi_{in}(x,-y)$]. Hard-wall reflection

requires $\psi=0$ at the step edge, and imposes a phase shift of π between the incoming and reflected wave. We therefore cannot expect this model to describe correctly either the phase of the Friedel oscillations or their amplitude in the immediate vicinity of a step edge, but it will be shown that the hard-wall approximation is still a useful approach for describing the observed oscillations.

A. Quasifree electrons

To illustrate the implications of the semielliptic Fermi contour of Be($10\bar{1}0$) on the shape of the charge-density oscillations we calculate the local density of states (LDOS) at ϵ_F:

$$\rho(\epsilon_F,\vec{r})=\int |\psi_{in}(\vec{r})+\psi_{out}(\vec{r})|^2\,\delta(\epsilon-\epsilon_F)\,d^2\mathbf{k}_{||}. \quad (3)$$

We first approximate the surface-state wave functions by plane waves and neglect the influence of the tunnel barrier (i.e., ρ is determined at $z=0$). Considering reflection from a hard-wall step at $y=0$, this reduces the total wave function $\psi=\psi_{in}+\psi_{out}$ to

$$\psi_{\mathbf{k}}(x,y)=\sqrt{2}\,\sin(k_y y)\exp(ik_x x). \quad (4)$$

The integration over the Fermi contour can be performed analytically and results in

$$\rho(\epsilon_F,y)=\frac{\sqrt{m_x^* m_y^*}}{\pi\hbar^2}[1-\cos(G_{\bar{A}}y)J_0(2k_1 y) + \sin(G_{\bar{A}}y)E_0(2k_1 y)] \quad (5)$$

(cf. Fig. 1 for the definition of the coordinate axes). Here m^* are the effective masses in x and y direction, k_1 is indicated in Fig. 1, $J_0(r)$ is the zeroth-order Bessel function, and $E_0(r)=1/(\pi)\int_0^{\pi}\sin(-r\sin\varphi)d\varphi$ is a Weber function.[42] $E_0(r)$ looks similar to J_0, and like the Bessel function it decreases proportional to $1/\sqrt{r}$ for large arguments. The same calculation for a step edge at $x=0$ leads to the result that was derived earlier for free electrons[6,41]

$$\rho(\epsilon_F,x)=\frac{\sqrt{m_x^* m_y^*}}{\pi\hbar^2}[1-J_0(2k_2 x)]. \quad (6)$$

From the shape and location of the Fermi contour it might be expected that surface-state electrons on Be($10\bar{1}0$) exhibit almost one-dimensional screening characteristics (the set of allowed k vectors is confined to a small triangular area around $\bar{\Gamma}$-$\bar{A}$). Indeed, when we consider two limiting cases it becomes clear that Eq. (5) describes a situation between purely one-dimensional and two-dimensional screening. For $G_{\bar{A}}\to 0$, Eq. (5) transforms into the two-dimensional free-electron result in Eq. (6), and for $k_1\to 0$ we obtain the one-dimensional Friedel oscillation

$$\rho_{1D}(y)=\frac{m}{\pi\hbar^2}[1-\cos(2k_{\bar{A}}y)]. \quad (7)$$

It can be seen from Eq. (5) the range of the Friedel oscillations on Be($10\bar{1}0$) ($\rho\propto 1/\sqrt{2kr}$) is the same as for a free two-dimensional electron gas. The most important difference between Be($10\bar{1}0$) and the free-electron case is the appearance of lattice periodic terms in the LDOS. It has been shown in Ref. 21 that the power spectrum of Eq. (5) displays a maximum at $k=G_{\bar{A}}$. In principle, the lattice-periodic term could serve as proof for the non-free character of the Friedel oscillations on Be($10\bar{1}0$). In practice, it is unfortunately impossible to demonstrate the presence of such lattice-periodic oscillations, because they cannot be separated from the topographic corrugation.

B. Anisotropy

Why do the experimental data show strong wave patterns emanating from the step edges that run parallel to [0100], while there are only very weak waves originating at the steps running parallel to [0001]? To explain this anisotropy we have to consider that the length of the reflecting step edges is finite. The calculation that was presented in the last paragraph has assumed infinite step length, and therefore the resulting wave amplitudes did not depend on the step orientation. An exact derivation of the wave functions in a scattering geometry with finite length steps is laborious and beyond the scope of this paper. We can, however, estimate the influence of finite step length by postulating that the scattering amplitude of a step segment scales as the projection of its geometric cross section onto a plane perpendicular to the wave vector of ψ_{in}. This projection is equivalent to scaling the outgoing wave function ψ_{out} with $\cos(\gamma)$ for a step at $y=0$ (a [0100] step). For a [0001] step we get $\psi_{out}\propto\sin(\gamma)\psi_{in}$. It follows that the charge *densities* due to scattering from both steps scale with the following factors:

$$S_{[0100]}(k_x,k_y)=\cos(\gamma)^2=\left[1+\left(\frac{k_2\cos(\varphi)}{k_{\bar{A}}-k_1\sin(\varphi)}\right)^2\right]^{-1}, \quad (8)$$

$$S_{[0001]}(k_x,k_y)=\sin(\gamma)^2=\left[1+\left(\frac{k_{\bar{A}}-k_1\cos(\varphi)}{k_2\sin(\varphi)}\right)^2\right]^{-1} \quad (9)$$

(γ and φ are indicated in Fig. 1). The anisotropy of the wave amplitudes at ϵ_F is given by the ratio of these two scaling functions integrated over all possible directions of the incoming wave vector:

$$R(\epsilon_F)=\frac{\int_0^{\pi}\sin[\gamma(\varphi)]^2 d\varphi}{\int_0^{\pi}\cos[\gamma(\varphi)]^2 d\varphi}. \quad (10)$$

With $k_1=0.29$ Å^{-1}, $k_2=0.39$ Å^{-1}, and $k_{\bar{A}}=0.89$ Å^{-1} we obtain $R(\epsilon_F)=0.16$. This result compares favorably with the experimental data for low bias voltage; the data shown in Fig. 6 indicate that $R(-10\text{ meV})\in[0.13,\ldots,0.2]$. We conclude that the observed anisotropy can be reasonably well explained by the geometric approximation. In spite of its simplicity this approximation highlights that the anisotropy of the charge-density oscillations on Be($10\bar{1}0$) relates directly to the location of the Fermi contour near $\bar{A}$. A [0100] step scatters efficiently because

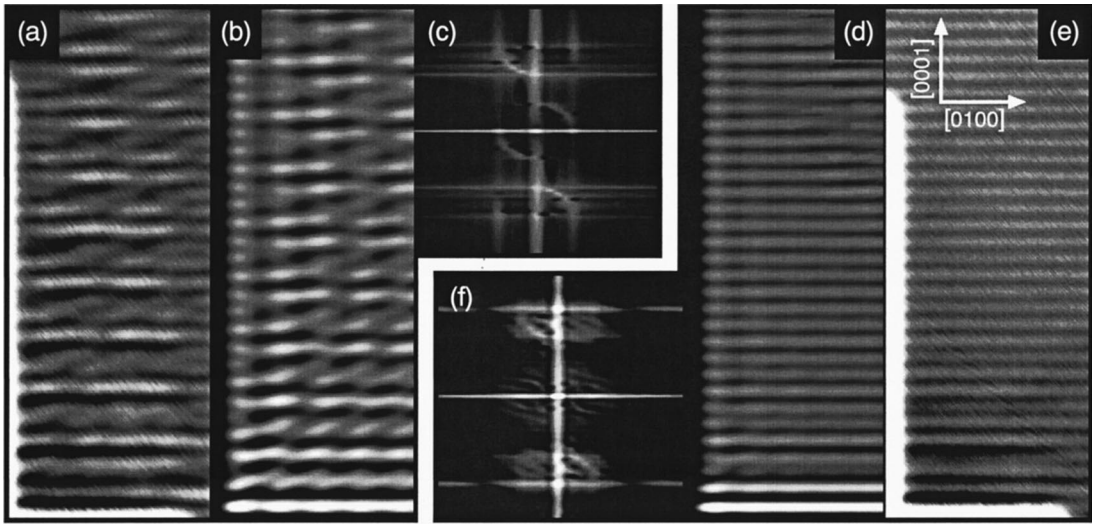

FIG. 9. Comparison between theory and experiment for charge-density oscillations near a kink. (a) Topographic STM data, recorded with $V_b=-10$ mV. (b) Calculated current image; the power spectrum of this image is shown in (c). (d) Theoretical current image for $V_b=-400$ mV. (e) Experimental data for the same bias voltage. (f) Power spectrum of the current image shown in (d).

the surface-state electrons are incident head-on. In contrast, at a [0001] step they are incident at grazing and scattering is inefficient. In addition to this geometric scaling there could, in principle, also exist intrinsic variations of the scattering cross section that derive from the electronic structure near differently oriented steps. It was, however, not possible to identify such intrinsic variations within the experimental error limits.

C. Bloch electrons

To describe the topographic images that are shown in Figs. 4–6 we have to extend our model. Specifically, we have to go back to the general wave function (2), which takes into account the presence of the tunnel barrier and higher order Bloch components. In general, the tunnel current is obtained by integrating $\rho(\epsilon,\mathbf{r})$ from ϵ_F to the bias voltage V_b. The exact expression for I_T depends on the shape of the tip wave functions. For the case of an *s*-wave tip (this case has been discussed extensively by Tersoff and Hamann[34]) the current is proportional to the integrated DOS at the tip position z_0:

$$I_{T,s}(\mathbf{r}_\parallel,z_0)=\text{const}\times\int_{\epsilon_F}^{\epsilon_F+V_b}\rho(\mathbf{r}_\parallel,z_0)\,d\epsilon. \tag{11}$$

The *s*-wave approximation predicts a strong suppression of higher-order Bloch components in STM images. It cannot explain that the atomic lattice corrugation on metals is resolved in the STM. This shortcoming has led Chen to propose that the probe tip should rather be described by a *p* or a *d* orbital.[43] In the following we shall use Chen's expression for a *d* wave tip,

$$I_{T,d}(\mathbf{r}_\parallel,z_0)=\text{const}\times\int|M_{d_z}|^2 d^2\mathbf{k}_{||}$$
$$=\text{const}\times\int\left|\frac{\partial^2\psi(\mathbf{r}_\parallel,z_0)}{\kappa^2\partial z^2}-\frac{1}{3}\psi(\mathbf{r}_\parallel,z_0)\right|^2 d^2\mathbf{k}_{||}. \tag{12}$$

Note that our experimental data do *not* display current variations; they show the topographic variation $\Delta z(x,y)$, which is needed to keep the tunnel-current constant. Δz is proportional to $1/(2\kappa)\ln(I_T)$. Only for the small z corrugation is it possible to linearize the logarithm and to compare the topographic data directly with calculated current images. We found this condition to be fulfilled in our experiments ($\Delta z\approx 0.1$ Å). The residual influence of linearization errors on the interpretation of the experimental topography images has been estimated in Ref. 22, and it has been concluded that this effect is negligible.

We now calculate the spatial dependence of the tunnel current for a scattering geometry containing two infinite steps at $x=0$ and $y=0$, respectively. As suggested by the experimental data we consider only Bloch components that contain reciprocal lattice vectors in the $\bar{\Gamma}$-$\bar{A}$ direction. The wave function in this geometry is

$$\psi(\mathbf{r}_\parallel,z)=\sqrt{2}\,\sin k_x x[\sin k_y y K_0(z)+a_1\sin(k_y+G_{\bar{A}})yK_1(z)$$
$$+a_{-1}\sin(k_y-G_{\bar{A}})yK_{-1}(z)+\cdots] \tag{13}$$

with the barrier factors

$$K_0(z)=\exp(-\sqrt{\kappa^2+\mathbf{k}_{||}^2}z),$$

$$K_{\pm1}(z)=\exp[-\sqrt{\kappa^2+(\mathbf{k}_{||}\pm\mathbf{G}_{\bar{A}})^2}z].$$

Inversion symmetry imposes the constraint $|a_{-1}|=|a_1|$. Here we set $a_{-1}=a_1$, i.e., we focus on the Bloch components, which are symmetric with respect to the position of the step edge. We proceed to determine the integrand of Eq. (12) up to the first order in a_1:

$$|M_{d_z}|^2=(1-\cos 2k_x x)L_0(z)((1-\cos 2k_y y)L_0(z)$$
$$+2a_1\{L_1(z)[\cos G_{\bar{A}}y-\cos(G_{\bar{A}}+2k_y)y]+L_{-1}(z)$$
$$\times[\cos G_{\bar{A}}y-\cos(G_{\bar{A}}-2k_y)y]\}), \tag{14}$$

with the modified barrier factors

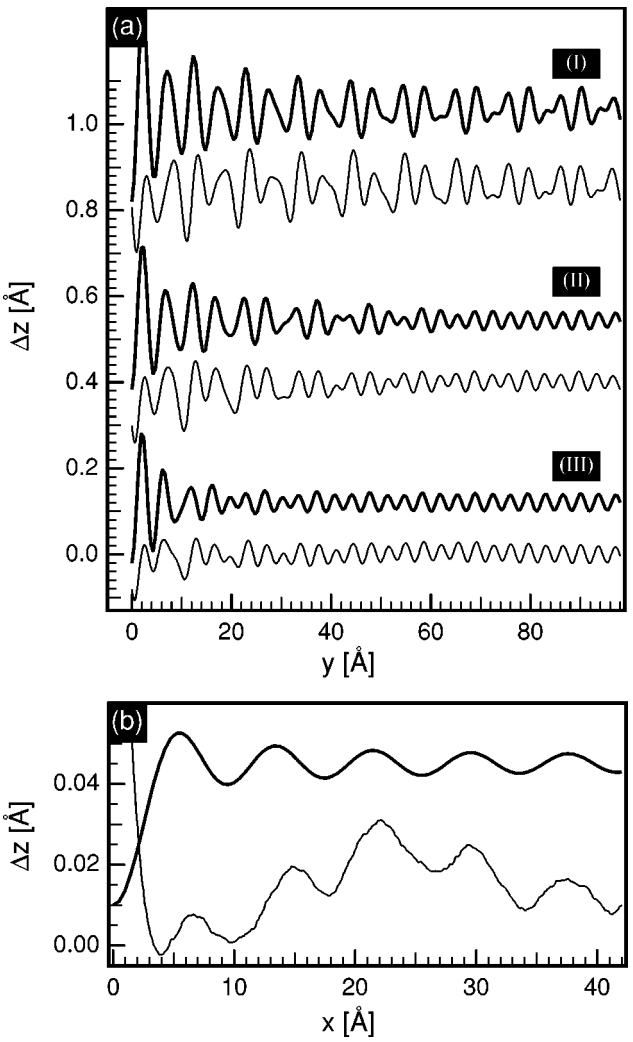

FIG. 10. Averaged line cuts illustrating the shape and range of the Friedel oscillations near a kink. Experimental data are plotted by thin lines and theoretical results by bold lines, respectively. (a) Cuts in the [0001] direction for three different sample bias voltages: -10 mV (I), -100 mV (II), and -300 mV (III). (b) Cuts in the [0100] direction for $V_b=-10$ mV.

$$L_0(z)=\left(\frac{\kappa^2+\mathbf{k}_{||}^2}{\kappa^2}-\frac{1}{3}\right)K_0(z),$$

$$L_{\pm 1}(z)=\left(\frac{\kappa^2+(\mathbf{k}_{||}\pm\mathbf{G}_{\bar{A}})^2}{\kappa^2}-\frac{1}{3}\right)K_{\pm 1}(z).$$

A tunnel current image is finally obtained by numerically evaluating Eq. (12). Typical results of such model calculations are displayed in Fig. 9. Figures 9(a) and 9(e) show experimental data for bias voltages of -10 and -400 mV. The model images for the same bias voltages are shown in Figs. 9(b) and 9(c). They were obtained using the parameters $a_1=-0.13$ and $z=5$ Å. Considering the simplicity of our model the overall agreement between theory and experiment is very satisfactory. The model image for low-bias voltage reproduces the distortion of the wave fronts emanating from a [0100] step due to the presence of a kink. For both bias voltages the range of the charge-density oscillations is correctly predicted. The shape of the oscillations in the calculated images was found to depend quite sensitively on the Bloch coefficient a_1. Our model can therefore be used to estimate rather accurately how much the surface-state wave functions on Be(10$\bar{1}$0) deviate from plane waves. Good agreement between model and experiment could be obtained for $a_1\in[-0.15,-0.1]$. Figures 9(c) and 9(f) display power spectra of the model images. These spectra highlight that a kink does indeed generate spectral weight in the ''tails'' of the semielliptic Fermi contour. Only a quarter-ellipse is visible, because the selection of one particular kink orientation breaks the symmetry with respect to the $\bar{\Gamma}$-$\bar{A}$ axis. Note that the experimental data shown in Fig. 2(d) display a similar asymmetry; there is more spectral weight in one tail of the semiellipses. Inspection of the corresponding topography image in Fig. 2(a) reveals that the main contribution to the charge-density oscillations is indeed provided by steps and kinks with the same orientation as the model kink shown in Fig. 9.

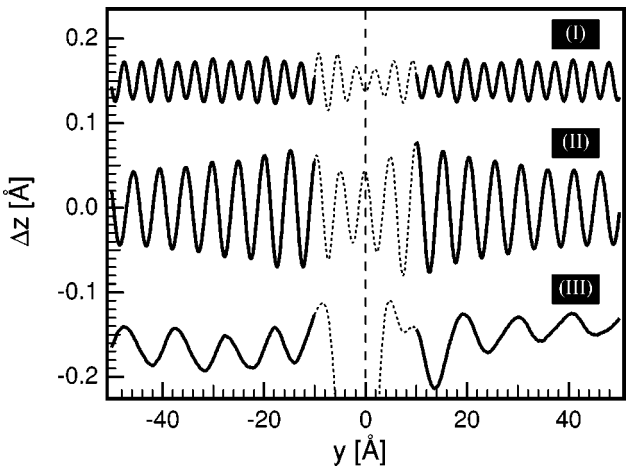

FIG. 11. Averaged line cuts across a [0100] step at $y=0$ for $V_b=-10$ mV. The cuts have been extracted from Fourier-filtered data and represent different spectral components of the wave pattern. (I) Lattice-periodic part; (II) free-electron component as shown in Fig. 5(b); (III) Bloch component, i.e., long-period oscillations as shown in Fig. 6(a).

To compare the model and experiment in more detail, and to illustrate the bias dependence of the waves, we have compiled several line cuts in Fig. 10. The line cuts were extracted from images like those shown in Fig. 9. All cuts are averaged over the whole width of the data set to minimize distortion by the kink. The amplitude of the theoretical curves (bold lines) was scaled to the experimental data (thin lines) at large distances from the step edge. Figure 10(a) shows three line cuts in the [0001] direction. It is evident that the model results agree rather well with the experiments. The most significant deviations occur in the vicinity of the step edge. This had to be expected because we have arbitrarily fixed the boundary conditions at the step edge for the model calculations. Because we cannot incorporate the geometric approximation for finite-step length into the wave functions (13) the theoretical current images do not correctly predict the observed anisotropy. Consequently, the amplitude of the waves originating at the [0001] step in Figs. 9(b) and 9(c) is much larger than in the experimental data. The finite-step length

can be taken into account for low-bias voltage simply by multiplying the line cuts that originate from a [0001] step with the geometric scaling factor $R(\epsilon_F)$. This scaling has been applied to the model data for $V_b=-10$ mV after normalizing the [0100] line cut with the same factor that was needed to adjust the amplitude of trace I in Fig. 10(a). The resulting line cut and the corresponding experimental data are shown in Fig. 10(b). Both cuts display a comparable wave amplitude suggesting that geometric scaling works rather well for this case.

So far we have focused on the amplitude of the Friedel oscillations. It should, however, be mentioned that the phases of these oscillations also contain information about the shape of the scattering potential. The hard-wall potential arbitrarily imposes a phase of π (i.e., a charge-density minimum) at the step edge. Therefore, the theoretical results of Figs. 9 and 10 had to be phase shifted to match the corresponding experimental data at large distances from the step edge. Although our calculation does not predict the phases of the Friedel oscillations, it is nevertheless interesting to look for phase information in the experimental data. This information must be extracted from Fourier-filtered images, because the wave pattern on Be$(10\bar{1}0)$ contains multiple periods that have to be considered separately. Figure 11 displays the result of such an analysis. The figure contains three averaged line cuts that have been taken across the [0100] step shown in Figs. 4–6. The data in the immediate vicinity of the step edge (dashed lines) have been distorted by the filtering process and should not be used to extract the phase. Trace I represents the lattice-periodic contribution of the observed wave pattern. This trace shows no evidence of phase distortion. It can be inferred that the lattice-periodic part of the Friedel oscillations is in phase with the ''true'' topographic corrugation due to bulk electronic states. Trace II shows the free-electron part of the oscillations. By extrapolating the phase from the flat terraces back to the step edge we obtain a phase of $0.3\pm0.1\pi$ for this trace. This means that the charge density almost reaches a maximum at the step-edge position but the wave crests are slightly shifted towards the step edge. The long-period oscillation (i.e., the spectral component at $G_{\bar{A}}-2k_F$) is shown in trace III. This trace deviates significantly from a strictly periodic wave train, and therefore it is not possible to determine a precise phase shift. The distortion of trace (III) relates to the weak intensity of this spectral component. It can be seen in Fig. 7(b) that the peak at $G_{\bar{A}}-2k_F$ is significantly broadened. Unless Fourier filtering is performed with a very steep and narrow passband this background will contribute to the wave form even in the filtered images. In spite of this limitation we can still say that the step-edge position roughly coincides with a minimum of the long-period oscillation. The phase inversion between traces II and III is consistent with our finding of a negative Bloch coefficient a_1.

After having discussed the scattering from step edges and kinks at some length we finally want to address the case of a point scatterer. Even if we approximate a point defect on Be$(10\bar{1}0)$ by a circular hard-wall potential, it is still a cumbersome task to determine the shape of the total wave functions. To obtain a rough idea about the shape of charge-density oscillations near scatterers with point symmetry we consider a hypothetical ''model'' defect, which scatters only specularly (i.e., every incoming wave is reversed). This case is admittedly a far cry from a real point defect, but it can be treated with the same approximations that were used in the last paragraph. We start with the wave functions

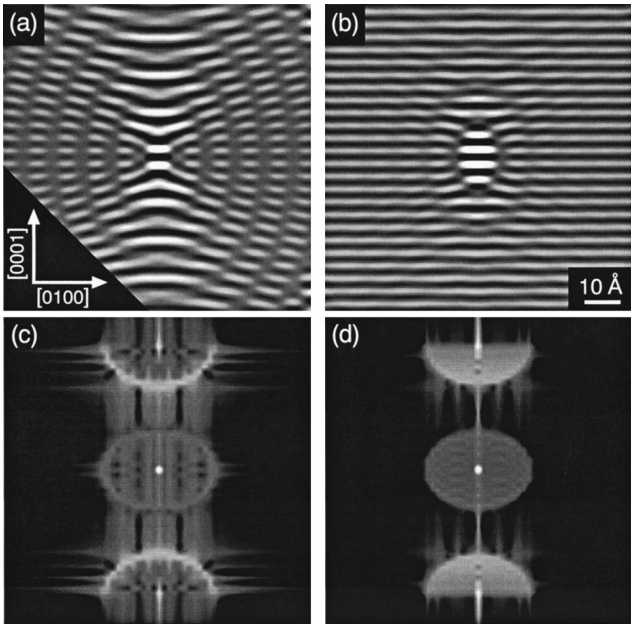

FIG. 12. Calculated current images showing charge-density oscillations near a ''model'' defect with point symmetry. (a) Energy-resolved oscillations near ϵ_F ($V_b=-10$ mV). (b) Integrated charge-density oscillations ($V_b=-400$ mV). (c) and (d) Power spectra of the current images shown above.

$$\psi(\mathbf{r}_\parallel,z)=\sin[\mathbf{k}_{||}\cdot\mathbf{r}_{||}]K_0(z)+a_1\sin[(\mathbf{k}_{||}+\mathbf{G}_{\bar{A}})\cdot\mathbf{r}_{||}]K_1(z)+a_1\sin[(\mathbf{k}_{||}-\mathbf{G}_{\bar{A}})\cdot\mathbf{r}_{||}]K_{-1}(z)+\cdots \quad (15)$$

and calculate the tunnel current up to first order in a_1. Figure 12 shows two examples of such current images for $a_1=-0.13$ and $z=5$ Å. Both images illustrate that the waves exhibit a negative curvature. In accordance with the experimental findings shown in Fig. 7 the wave crests that appear in Figs. 12(a) and 12(b) bend away from the point scatterer. The amplitude and range of the charge-density oscillations is, however, much larger in Fig. 12(a) than in the experiment, because the approximation (15) strongly overestimates the scattering amplitude of a point defect. A real point defect scatters into all directions, which correspond to allowed k vectors. The superposition of the scattered wavelets will lead to partial cancellation of the charge-density oscillations, and thus the amplitude and range of the resulting oscillations will be reduced. The Fourier images that are shown in Fig. 12(c) and 12(d) illustrate that a point-symmetric scatterer indeed promotes an oscillation pattern that displays a full replica of the Fermi contour in its power spectrum. The additional ellipse in the center corresponds to the long periodic waves that we have observed in the experiments. The strength of the centered ellipse scales with a_1. As we have expected, the multiperiodicity directly follows from the fact that surface-state electrons on Be$(10\bar{1}0)$ have to be described by Bloch functions.

In summary, we have shown using a simple model how the main features of the experimental STM data reflect directly the band structure of the surface state on Be($10\bar{1}0$). These experiments have established that the interaction between surface-state electrons and the lattice potential can be probed using STM. They have demonstrated that STM studies of charge-density oscillations are by no means restricted to free-electron systems. We anticipate that the experimental methods and analysis techniques that have been described here can also be successfully applied to the study of more complex electron-lattice and electron-phonon interactions on surfaces.

ACKNOWLEDGMENTS

The authors acknowledge helpful discussions with G. D. Mahan, D. M. Eigler, and R. Berndt. Ph.H. thanks the Alexander von Humboldt Stiftung for support. This work has been supported in part by the National Science Foundation under Grant No. NSF-95-10132.

*Present address: Institute for Storage Ring Facilities, University of Århus, Ny Munkegade, 8000 Århus C, Denmark.

[1] J. Friedel, Nuovo Cimento Suppl. **7**, 287 (1958).
[2] I. Adawi, Phys. Rev. **146**, 379 (1966).
[3] A. M. Gabovich, L. G. Il'chenko, E. A. Pashitskii, and Yu. A. Romanov, Zh. Eksp. Teor. Fiz. **75**, 249 (1978) [Sov. Phys. JETP **48**, 124 (1978)].
[4] K. H. Lau and W. Kohn, Surf. Sci. **75**, 69 (1978).
[5] W. Kohn, Phys. Rev. Lett. **2**, 393 (1959).
[6] M. F. Crommie, C. P. Lutz, and D. M. Eigler, Nature (London) **363**, 524 (1993).
[7] Y. Hasegawa and Ph. Avouris, Phys. Rev. Lett. **71**, 1071 (1993).
[8] M. F. Crommie, C. P. Lutz, and D. M. Eigler, Science **262**, 218 (1993).
[9] P. T. Sprunger, L. Petersen, E. W. Plummer, E. Laegsgaard, and F. Besenbacher, Science **275**, 1764 (1997).
[10] J. T. Li, W. D. Schneider, and R. Berndt, Phys. Rev. B **56**, 7656 (1997).
[11] M. Schmid, W. Hebenstreit, P. Varga, and S. Crampin, Phys. Rev. Lett. **76**, 2298 (1996).
[12] M. C. M. M. van der Wielen, A. J. A. van Roij, and H. van Kempen, Phys. Rev. Lett. **76**, 1075 (1996).
[13] M. A. Ruderman and C. Kittel, Phys. Rev. **96**, 99 (1954); T. Kasuya, Prog. Theor. Phys. **16**, 45 (1956); K. Yosida, Phys. Rev. **106**, 893 (1957).
[14] P. Grünberg, R. Schreiber, Y. Pang, M. B. Brodsky, and H. Sowers, Phys. Rev. Lett. **57**, 2442 (1986).
[15] S. S. P. Parkin, R. Bhadra, and K. P. Roche, Phys. Rev. Lett. **66**, 2152 (1991).
[16] J. Unguris, R. J. Celotta, and D. T. Pierce, Phys. Rev. Lett. **67**, 140 (1991).
[17] W. Weber, R. Allenspach, and A. Bischof, Europhys. Lett. **31**, 491 (1995).
[18] P. Bruno and C. Chappert, Phys. Rev. Lett. **67**, 1602 (1991).
[19] F. Herman and R. Schrieffer, Phys. Rev. B **46**, 5806 (1992).
[20] M. Stiles, Phys. Rev. B **48**, 7238 (1993).
[21] Ph. Hofmann, B. G. Briner, M. Doering, H.-P. Rust, E. W. Plummer, and A. M. Bradshaw, Phys. Rev. Lett. **79**, 265 (1997).
[22] B. G. Briner, Ph. Hofmann, M. Doering, H.-P. Rust, E. W. Plummer, and A. M. Bradshaw, Europhys. Lett. **39**, 67 (1997).
[23] M. Y. Chou, P. K. Lam, and M. L. Cohen, Phys. Rev. B **28**, 4179 (1983).
[24] L. I. Johansson, H. I. P. Johansson, J. N. Andersen, E. Lundgren, and R. Nyholm, Phys. Rev. Lett. **71**, 2453 (1993).
[25] R. A. Bartynski, E. Jensen, T. Gustafsson, and E. W. Plummer, Phys. Rev. B **32**, 1921 (1985).
[26] E. V. Chulkov, V. M. Silkin, and E. N. Shirykalov, Surf. Sci. **188**, 287 (1987).
[27] V. M. Silkin and E. V. Chulkov, Fiz. Tverd. Tela (Leningrad) **37**, 2795 (1995) [Phys. Solid State **37**, 1540 (1995)].
[28] Ph. Hofmann, K. Pohl, R. Stumpf, and E. W. Plummer, Phys. Rev. B **53**, 13 715 (1996).
[29] Ph. Hofmann, R. Stumpf, V. M. Silkin, E. V. Chulkov, and E. W. Plummer, Surf. Sci. **355**, L278 (1996).
[30] P. S. Weiss and D. M. Eigler, in *Nanosources and Manipulation of Atoms under High Fields and Temperatures*, Vol. 235 of NATO Advanced Study Institute, Series E: Applied Sciences, edited by V. T. Binh *et al.* (Kluwer Academic, Dordrecht, 1993), p. 213.
[31] H.-P. Rust, J. Buisset, E. K. Schweizer, and L. Cramer, Rev. Sci. Instrum. **39**, 999 (1997).
[32] R. E. Thomson, U. Walter, E. Ganz, J. Clarke, A. Zettl, P. Rauch, and F. J. DiSalvo, Phys. Rev. B **38**, 10 734 (1988).
[33] L. Petersen, P. T. Sprunges, Ph. Hofmann, E. Laegsgaard, B. G. Brines, M. Doering, H.-P. Rust, A. M. Bradshaw, F. Besenbacher, and E. W. Plummer, Phys. Rev. B **57**, R6858 (1998).
[34] J. Tersoff and D. R. Hamann, Phys. Rev. Lett. **50**, 1998 (1983); Phys. Rev. B **31**, 805 (1985).
[35] G. Hörmandinger, Phys. Rev. B **49**, 13 897 (1994).
[36] V. A. Ukraintsev, Phys. Rev. B **53**, 11 176 (1996).
[37] Room-temperature ARUPS data indicate that the band edge of the surface state is located approximately 330 meV below ϵ_F. *Ab initio* calculations suggest 400 meV for the position of this band edge. This value has not been checked independently using STM. Because the STM data for the dimensions of the Fermi contour agree much better with theory than with ARUPS we use the calculated band-edge position for the calculations in Sec. IV.
[38] C. Kittel, in *Solid State Physics*, edited by F. Seitz, D. Turnbull, and H. Ehrenreich (Academic, New York, 1968), Vol. 22, p. 1.
[39] M. Doering, J. Buisset, H.-P. Rust, B. G. Briner, and A. M. Bradshaw, Faraday Discuss. **105**, 163 (1996).
[40] R. Ferro, At. Energy **4**, 63 (1973).
[41] Ph. Avouris, I.-W. Lyo, R. E. Walkup, and Y. Hasegawa, J. Vac. Sci. Technol. B **12**, 1447 (1994).
[42] G. N. Watson, *Theory of Bessel Functions* (Cambridge University Press, Cambridge, England, 1952).
[43] C. J. Chen, Phys. Rev. Lett. **65**, 448 (1990); Phys. Rev. B **42**, 8841 (1990).